Chapter 5 – NUMERICAL SOLUTIONS FOR THE CAWAPI CONFIGURATION ON STRUCTURED GRIDS AT NLR, THE NETHERLANDS

by

Okko J. Boelens, Stephanus P. Spekreijse,
Harmen A. Sytsma and Koen M.J. de Cock

5.1 SUMMARY

Accurate and cost-effective Computational Fluid Dynamics (CFD) methods play an increasingly important role, even in the support of fighter aircraft operations. Prior to the deployment of such CFD methods they should be well validated and evaluated against state-of-the-art wind-tunnel and/or flight test data. The Cranked-Arrow Wing Aerodynamics Project (CAWAP) provided the CFD community with an excellent database for validation and evaluation. Initiated by NASA, the Cranked-Arrow Wing Aerodynamics Project International (CAWAPI) was started as a follow-on project of CAWAP. The National Aerospace Laboratory NLR participated in this project using the in-house developed flow simulation system ENFLOW, which includes both grid generation tools and a flow solver. NLR applied (semi-automatic) grid generation tools to generate a structured (multi-block) grid. Steady flow simulations for all seven CAWAPI flight conditions are performed employing the flow solver ENSOLV. Results obtained for flight condition 7, 19 and 25 are discussed. The focus of this discussion is on a comparison of the measured and simulated flow features. It is shown that the understanding of NLR's structured (multi-block) grid generation algorithm and the confidence in the application of its flow simulation method to complex fighter configurations increased significantly by participating in CAWAPI.

5.2 INTRODUCTION

Application of Computational Fluid Dynamics (CFD) methods to support the operation of fighter aircraft requires sufficient accuracy (fidelity) and cost-effectiveness of these methods compared to alternatives such as wind-tunnel tests or flight tests. Two envisaged applications are the assessment of stability and control characteristics and the assessment of changes in aircraft loads due to new store configurations. By using CFD methods the number of flight conditions that need to be flown in a flight test certification program can be optimized and potentially dangerous flight conditions can be identified beforehand. To enable application of CFD methods for such purposes with confidence, the methods should be well validated and evaluated against state-of-the-art wind tunnel and/or flight test data.

The Cranked-Arrow Wing Aerodynamics Project (CAWAP) (see Chapter 3 and [5-1]) provided the CFD community with an excellent database for validation and evaluation purposes. This project focused on the understanding of flow phenomena encountered on a cranked-arrow wing relevant to advanced supersonic fighter and transport aircraft. Initiated by NASA, the Cranked-Arrow Wing Aerodynamics Project International (CAWAPI) was started as a follow-on project.

The National Aerospace Laboratory NLR participated in this task group using the in-house developed flow simulation system ENFLOW, which includes both grid generation tools and a flow solver. The application of the NLR ENFLOW flow simulation system to the CAWAPI test cases is the main subject of this chapter. Based on the IGES file containing the water tight geometry description of the F-16XL (see Chapter 4),

a structured (multi-block) grid was generated at NLR using a grid mapping technique. The grids used in simulations will be discussed in Section 5.3 (see also Chapter 4). Section 5.4 will discuss the important features of the flow solver ENSOLV, which is part of the simulation system ENFLOW. Section 5.5 will discuss some of the results obtained at NLR. The focus will be on a comparison of the measured and simulated flow features. A section with conclusions (Section 5.6) completes this chapter. Both the grid generation process and the flow simulation process employed by NLR will be assessed with respect to their Technology Readiness Level.

5.3 GRID

At the Netherlands National Aerospace Laboratory NLR a family of structured (multi-block) grids has been generated using a Cartesian grid mapping technique. The following grids which are part of this family of structured (multi-block) grids have been used by NLR in CAWAPI:

- The baseline structured grid around the half-span full-scale model of the F-16XL consisting of 1903 blocks, 14,750,720 grid cells and 17,014,119 grid points.
- The baseline structured grid with a reduced number of blocks. The merging step resulted in a reduction of the number of blocks from 1903 to 216.
- A structured grid around the full-scale model of the F-16XL consisting of 3806 blocks, 29,501,440 grid cells and 34,028,238 grid points. This grid has been generated by mirroring the baseline structured grid around the half-span full-scale model of the F-16XL with respect to the symmetry plane.

Further details on the grid generation method and the baseline structured grid around the half-span full-scale model of the F-16XL can be found in Chapter 4.

5.4 FLOW SOLVER

5.4.1 General Description

The flow solver ENSOLV, which is part of NLR's flow simulation system ENFLOW [5-2], is capable of solving the Euler and Navier-Stokes equations on multi-block structured grids for arbitrary configurations. The configuration can be either fixed or moving relative to an inertial reference frame, and can be either rigid or flexible.

The flow equations are cast into a full conservation form employing the density ρ, the components of the momentum vector $\rho\mathbf{u}$ and the total energy per unit volume ρE as dependent variables. The equations are non-dimensionalized using the free-stream static pressure, the free-stream density, the free-stream temperature and a reference length (for example the reference wing chord).

The equations in full conservation form are discretized in space by a second-order accurate, cell-centred, finite-volume method, using multi-block structured grids, central differences, and matrix artificial diffusion. The artificial diffusion consists of a blending of second-order and fourth-order differences with a Jameson-type shock sensor for the basic flow equations and a TVD discontinuity sensor for the turbulence model equations.

For steady flow simulations, the discretized time-dependent system of equations is integrated toward the steady-state solution using a five-stage explicit Runge-Kutta scheme. Local-time stepping, implicit residual averaging and multi-grid acceleration techniques are applied.

For time-accurate simulations, the flow solver uses the dual-time stepping scheme, where for each time-step the time-dependent flow equations are integrated in pseudo-time toward a steady-state solution in a similar way as in the steady flow simulation using the same acceleration techniques.

5.4.2 Turbulence Model

Several turbulence models are present in the flow solver ENSOLV, including the Turbulent Non-Turbulent (TNT) k-ω model [5-4] [5-5], the EARSM model [5-5] and a hybrid RANS-LES model for eXtra-Large Eddy Simulation (X-LES) [5-6] [5-7].

For all simulations in the present study, the TNT k-ω model, which is a variant of the Wilcox k-ω model, is employed. The equations of the model are slightly modified by the introduction of a 'cross diffusion' term [5-3]. This modification has been introduced to resolve the dependency of the free-stream-valued of ω. The model is also extended with a global correction for vortical flows [5-4] [5-5]. It is well known that the standard model, as with most other two-equation models, over predicts the eddy viscosity within the vortex core which leads to exaggerated diffusion of vorticity. As a consequence the details of the vortex core are lost and low suction peaks with wide vortex bases are a characteristic of the solution. The enhanced model[18] controls the production of turbulent kinetic energy and hence eddy viscosity through an increase in the production of dissipation (ω) within regions of highly rotational flow. A suitable sensor has been used to distinguish between shear layers and vortex cores. This sensor is the ratio between the magnitude of strain-rate and vorticity tensor. In shear layers, the velocity gradient is dominated by the gradient in the normal direction, which results in a ratio of approximately one, while in vortex cores, where the flow experiences pure rotation, the ratio is much less than one. This approach has proven to be effective in producing surface pressure profiles on simple delta wings in good agreement with those of experimental data [5-4] [5-5].

In addition, to remove the singular behaviour of ω at solid boundaries, the equations of the k-ω model are reformulated such that instead of ω the quantity $\tau = 1/(\omega+\omega_0)$ is used. Here ω_0 is a positive constant (default value $\omega_0 L_{ref}/u_\infty = 20$, with U_∞ the free-stream velocity and L_{ref} the reference length). Finally, the source terms in the k-ω equations are treated explicitly, while a separate time-step is used for the k-ω equations to enhance the efficiency of the scheme.

At the solid boundaries, both k and τ are set to zero. To prevent unphysical high values of k near stagnation points, the production term in the k-equation has been limited to a maximum of 20 times the dissipation term in the k-equation.

At the 'inflow' parts of the far-field boundary, the free-stream values of the turbulent variables are computed from the free-stream turbulent Reynolds number (0.01 in the present simulations) and the free-stream dimensionless turbulent kinetic energy ($k/u_\omega^2 = 10^{-6}$ in the present simulations).

All simulations were run in fully turbulent mode.

5.4.3 Boundary Conditions

At the F-16XL geometry, a no-slip viscous flow condition (Navier-Stokes adiabatic solid wall) has been employed. For the upstream, top, bottom and side far-field faces, a free-stream boundary condition based on Riemann invariants of the locally linearized one-dimensional Euler equations has been used. Since the flow at these faces is subsonic, the value of the 'incoming' Riemann invariants is computed using the free-stream values. The remaining invariants are extrapolated from the computational domain. A free-stream boundary condition

based on the extrapolation of the pressure has been used at the downstream far-field boundary. For the simulations on the grid around the half-span full-scale model of the F-16XL a symmetry boundary condition has been used at the symmetry plane. For this boundary condition the grid does not necessarily need to be orthogonal to the symmetry plane. Finally, at the inlet duct exit plane (engine inlet) a boundary condition with a prescribed normalized static pressure p/p_∞ is used, whereas at the mixing plane (engine exit) a boundary condition with a prescribed normalized total pressure $p_t/p_{t,\infty}$ and total temperature $T_t/T_{t,\infty}$ is applied.

5.4.4 Details of Simulations

All simulations were performed as steady flow simulations. A Full Multi-Grid (FMG) scheme (grid sequencing) was used to compute the solution on the three grid levels. The solution on a coarse level is used as initial solution on the next-finer level. The number of iterations on each grid level is shown in Table 5-1. The Full Approximation Storage (FAS) multi-grid scheme is used to compute the solution on a specific grid level. Two FAS multi-grid levels were used. The simulations were performed on two processors of NLR's NEC SX5/8B vector computer. Four orders of convergence were obtained for the root mean square norms. Computational details of the simulations are shown in Table 5-1.

Table 5-1: Computational Details of the Simulations

			Computational Wall-Clock Time (Use 2 processors of NLR's SX5/8B)	
	Number of Grid Cells	Number of Iterations	Baseline Structured Grid (see Section 5.3)	Baseline Structured Grid with a Reduced Number of Blocks (see Section 5.3)
4h-grid level	230,480	1500	4h55m	1h00m
2h-grid level	1,843,840	900	12h18m	2h41m
h-grid level	14,750,720	1200	45h31m	12h50m
Total			62h44m	16h33m

Note that, since larger block dimensions result in an increase of the vector length, merging the blocks resulted in a significant reduction of the required computational time. The computation time obtained with the baseline grid with a reduced number of blocks allowed the computation of all flight conditions well within one weekend.

5.5 COMPARISON OF THE MEASURED AND SIMULATED FLOW FEATURES

5.5.1 Flight Test Cases

At NLR simulations have been performed for all flight conditions on the grid around the half-span full-scale model, except for flight condition 50 and 51 for which the grid around the full-scale model was employed.

The data obtained during the flight tests (see Chapter 3 and [5-1]) comprised surface pressure measurements, both along butt lines (BL) and fuselage stations (FS), boundary layer measurements at four positions on the left wing, skin friction measurements at the FS330 station on the left wing and surface flow visualizations using tufts. The data available for each flight condition is shown in Table 5-2.

Table 5-2: Flight Test Data (A = Available, NA = Not Available)

Flight Condition	Surface Pressure Measurements	Boundary Layer Profiles	Skin Friction Measurements	Surface Flow Visualization
7	NA (Use flight condition 35 and flight condition 49 [5-1])	A	NA	A
19	NA	NA	A	A
25	A	NA	NA	A
46	A	NA	NA	A
50	A	NA	NA	A
51	A	NA	NA	A
70	A	NA	NA	A

Based on the data availability and the notion that flight condition 7 and flight condition 19 are practically identical, the assessment of the results presented here will be based on these two flight conditions. By combining the data of these two flight conditions, a fairly complete picture of the flow features can be drawn. In addition, for completeness a comparison of surface pressure measurements and the surface flow visualizations using tufts will be presented for flight condition 25.

The results of other flight conditions such as the transonic flow case (flight condition 70) are presented in Chapter 16.

The engine parameters associated with these flight conditions (see Chapter 3) are displayed in Table 5-3. The table also shows the parameters for the engine boundary conditions (see Section 5.4.3), which are used in the simulations.

Table 5-3: Engine Parameters

	Inlet duct Exit					Mixing plane			
Flight condition	T_s, °R	p_s, psia	u, ft/s	M	p/p_∞	T_t, °R	p_t, psia	$T_t/T_{t,\infty}$	$p_t/p_{t,\infty}$
7	498.0	11.00	379.6	0.347	*0.900*	1050.0	23.00	*2.058*	*1.764*
19	485.8	10.20	345.8	0.320	*1.009*	1050.0	21.50	*2.119*	*1.945*
25	470.1	8.72	474.8	0.447	*0.863*	1209.0	26.30	*2.474*	*2.498*
46	443.6	5.85	404.3	0.390	*1.026*	1045.0	14.80	*2.285*	*2.148*
50	440.0	5.16	483.3	0.470	*0.905*	1154.0	16.95	*2.567*	*2.611*
51	431.8	5.19	468.6	0.460	*0.910*	1146.0	16.74	*2.546*	*2.568*
70	519.0	10.65	464.7	0.416	*1.736*	1200.0	30.00	*2.299*	*2.675*

5.5.2 Assessment of the Results

Before looking in detail to the results, first the large-scale vortical flow structure above the wing is discussed. Figure 5-1 shows an iso-surface of the vorticity magnitude for flight condition 7. The level of the vorticity magnitude equals 250 Hz. The vortical flow structure consists of several vortices, i.e.:

i) The inner wing primary vortex originating from the wing leading edge inboard of the crank;

ii) Outer wing vortex originating from the wing leading edge outboard of the crank;

iii) The air dam vortex originating form the air dam at wing upper surface;

iv) The missile vortices originating from the missile fins; and

v) The fuselage vortex.

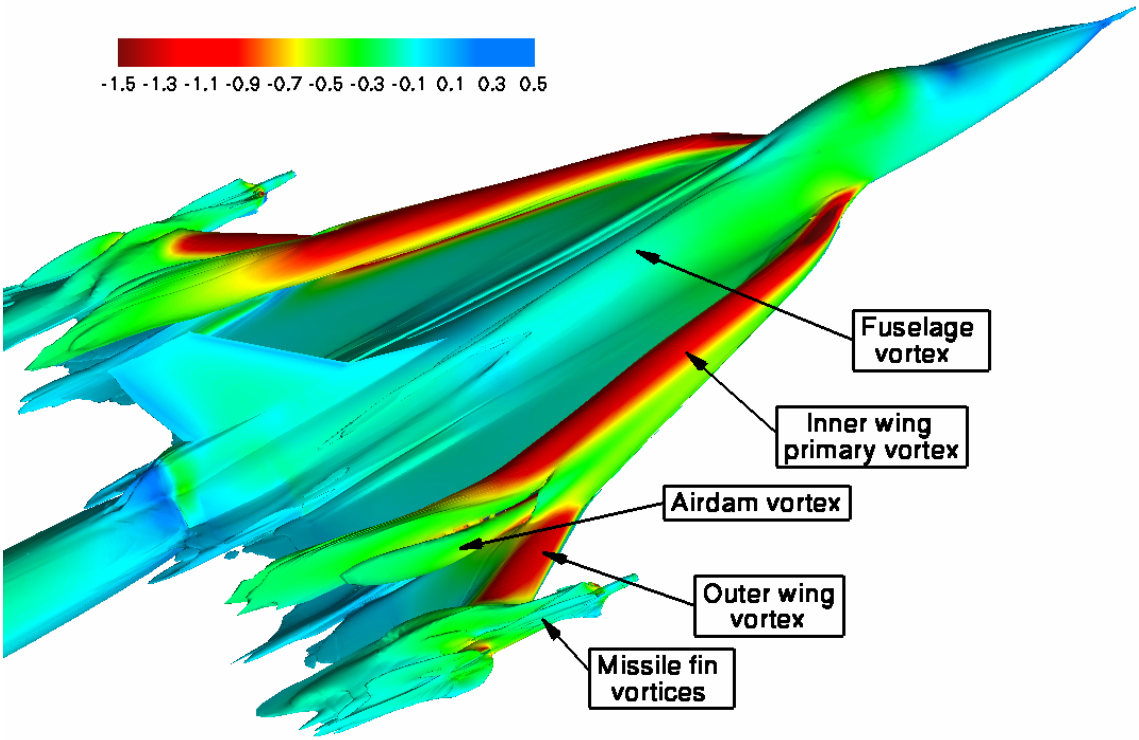

Figure 5-1: Iso-Surface (Level Equals 250 Hz) of Vorticity Magnitude for Flight Condition 7 (α = 11.89°, M = 0.304 and Re = 44.40 x 10^6). The vortices are colored by the pressure coefficient C_p.

In addition to these vortices other vortical structures, such as for example the inner wing secondary vortex, are present. All flight conditions characterized by vortical flow exhibit a similar vortical flow structure, although the strength and location of the vortices may differ. As can be seen in Figure 5-1, both the inner wing primary vortex and the outer wing vortex result in a region of high suction downstream of the leading edge.

This behaviour is also evident in the figures showing the sectional surface pressure coefficient at different butt line and fuselage stations. Figure 5-2 shows the sectional surface pressure coefficient for flight condition 25, whereas Figure 5-3 shows this coefficient for flight condition 7 as well as flight condition 19. For the flight condition 25 the simulation data is compared with the actual flight test data for this flight conditions. Since, however, for both flight condition 7 and flight condition 19 no surface pressure data is available, it was agreed within CAWAPI to use data from two neighbouring flight conditions, which are also recommended for comparison in [5-1]. These flight conditions are flight condition 34 (α = 13.50°, M = 0.370 and Re = 40.05 x 10^6) and flight condition 49 (α = 13.00°, M = 0.420 and Re = 38.97 x 10^6).

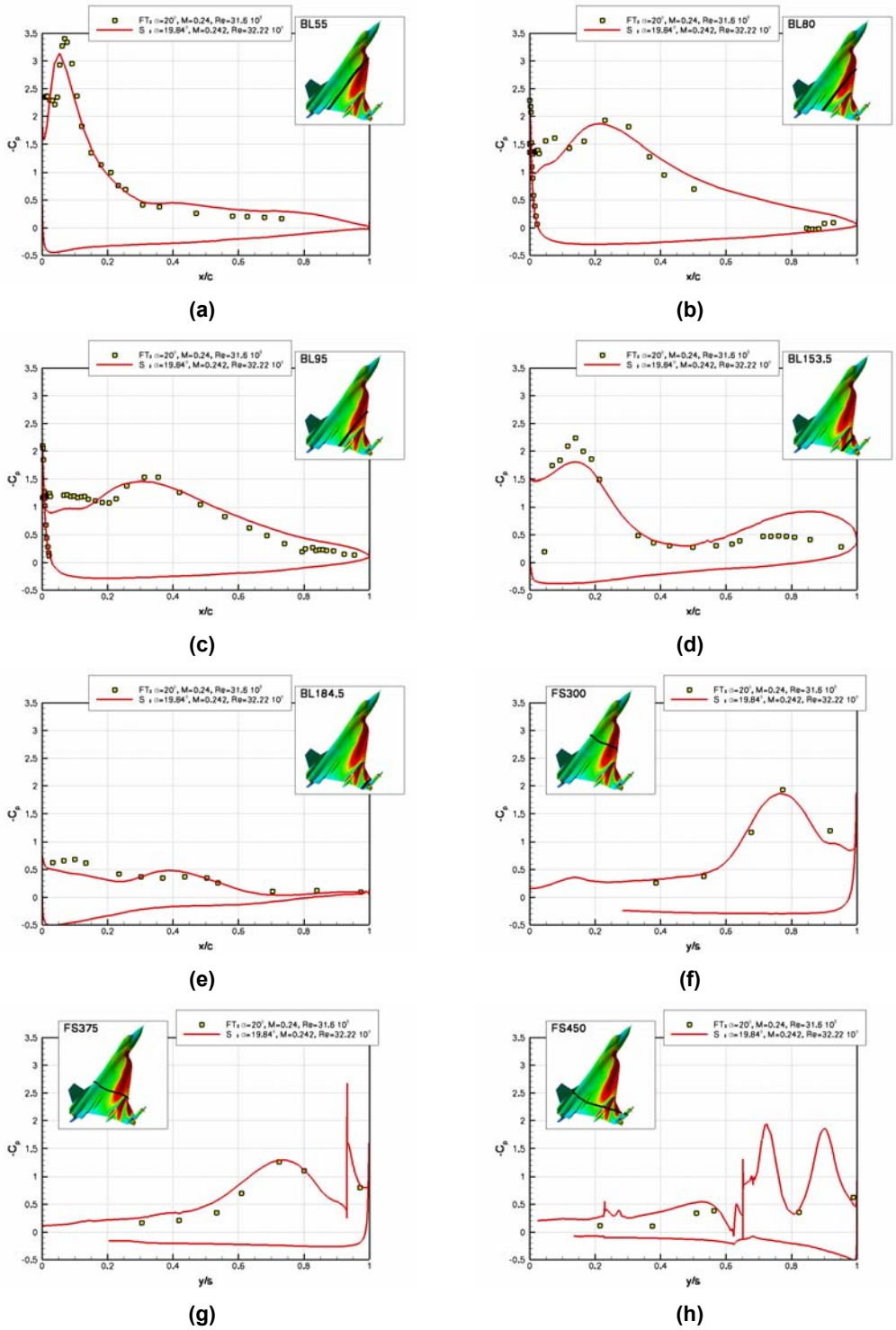

Figure 5-2: Surface Pressure Coefficient for Flight Condition 25 (α = 19.84°, M = 0.242 and Re = 32.22 x 10^6) along Butt Lines: (a) BL55; (b) BL80; (c) BL 95; (d) BL153.5 and (e) BL184.5; and Fuselage Stations: (f) FS300; (g) FS375; and (h) FS450.

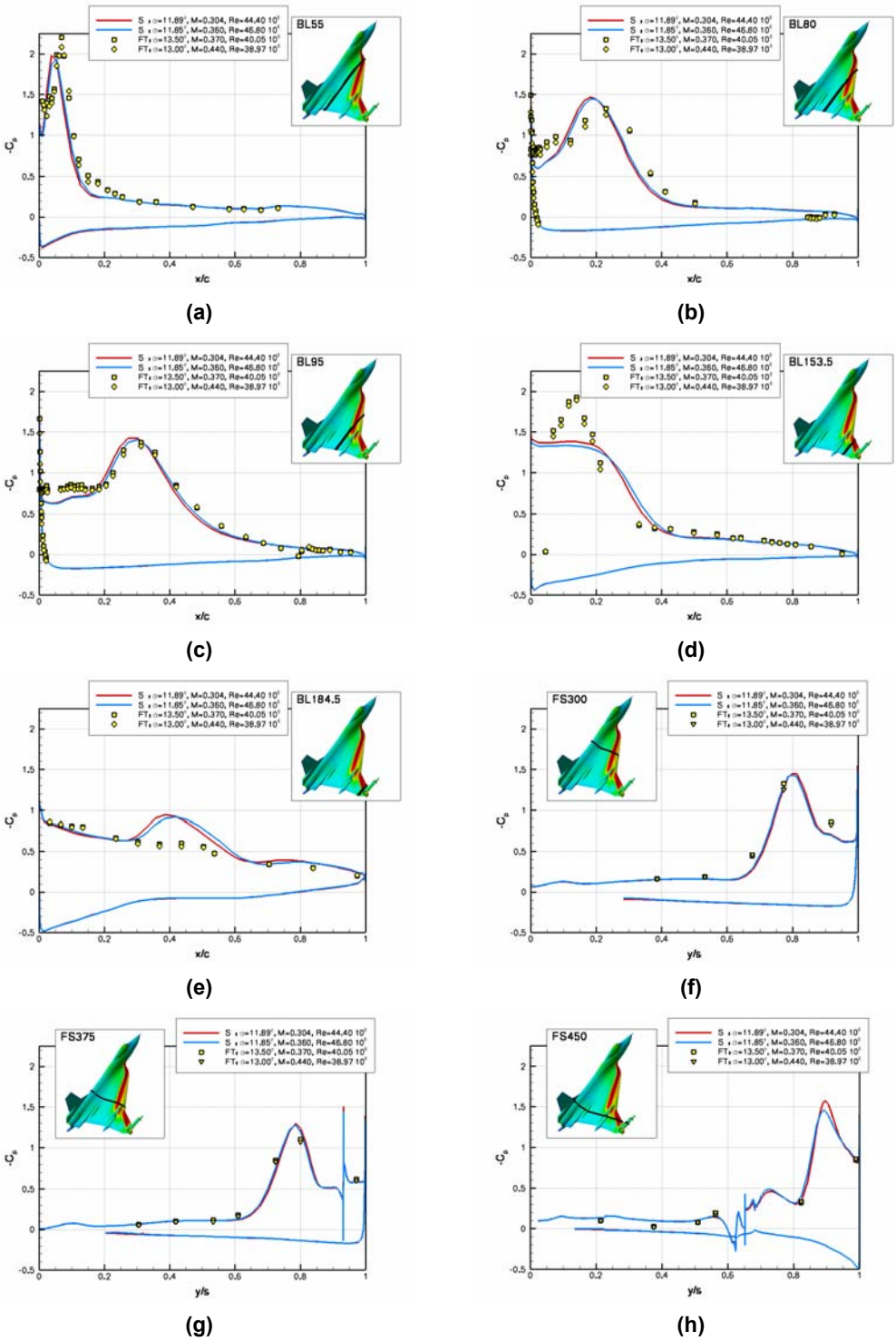

Figure 5-3: Surface Pressure Coefficient for Flight Condition 7 (α = 11.89°, M = 0.304 and Re = 44.40 x 10^6) and Flight Condition 19 (α = 11.85°, M = 0.360 and Re = 46.80 x 10^6) along Butt Lines: (a) BL55; (b) BL80; (c) BL 95; (d) BL153.5; and (e) BL184.5; and Fuselage Stations: (f) FS300; (g) FS375; and (h) FS450.

Surface pressure measurements are performed using 326 static pressure ports, both flush and in stream wise belts. 337 pressure ports are plumbed in the aircraft structure. These ports are arranged along butt lines and fuselage stations. During the flight tests, only 280 ports on the upper surface and 46 ports on the lower surface proved reliable.

Figure 5-2 and Figure 5-3 show that the agreement between flight tests and simulations is generally good. In addition, Figure 5-3 shows that the difference in surface pressure coefficient for flight condition 7 and flight condition 19 is small, as expected.

For all flight conditions the suction peak associated with inner wing primary vortex is predicted well, see Figure 5-2 (a), (b), (c), (f) and (g) and Figure 5-3 (a), (b), (c), (f) and (g). Since the flight test data is obtained at a higher angle of attack, a lower suction peak is to be expected in the simulations. The peak obtained by the simulations is also slightly more forward on the wing than the peak observed during the flight tests. The suction peak of the inner wing secondary vortex is, however, under predicted. This vortex also starts some distance downstream of the wing apex. The formation of the inner wing secondary vortex is postponed by the relatively coarse grid in the wing apex region.

On the part of the wing outboard of the crank, for flight condition 25 a pressure peak associated with the air dam vortex is observed. This vortex gives rise to a much higher pressure peak than observed during the flight tests; see Figure 5-2 (d) on the aft part of the wing. In addition, a pressure peak associated with the outer wing vortex is present. This pressure peak is under predicted in the simulations; see Figure 5-2 (d). Going outboard the difference between the simulation and the flight test becomes less pronounced; see Figure 5-2 (e). The agreement between the simulation and the flight test is good for all fuselage stations.

For flight condition 7 and flight condition 19, the pressure peak associated with the air dam vortex is much smaller; see Figure 5-3 (h). No influence of the air dam vortex is visible on the aft part of the wing; see Figure 5-3 (d). The outer wing vortex also results in a suction peak. Whereas in the flight tests a clear peak is observed, the simulations show a pressure peak that is rather flat in the part of the wing just outboard of the crank; see Figure 5-3 (d). Going outboard the pressure peak associated with the outer wing vortex, however, is over predicted; see Figure 5-3 (e). Once more, the agreement between the simulation and the flight test is good for all fuselage stations.

With respect to the turbulence model, it should be noted that the global correction for vortical flows (see Section 5.4.2) has primarily been validated for the primary vortex on simple sharp-edged delta wings [5-4] [5-5]. For the inner wing primary vortex, originating from the relatively sharp leading edge, the model results in a good prediction of the suction peak. However, the inner wing secondary vortex originates from a more complex boundary layer separation underneath the inner wing primary vortex. Despite the correction for vortical flows, which switches on in all vortical flow structures, the suction peak associated with the inner wing secondary vortex is under predicted. Inspection of the grid showed that in the region where the secondary vortex resides the grid is relatively coarse. This grid coarseness, especially in the apex region, is most probably the reason for the weaker agreement between the flight tests and the simulations for the inner wing secondary vortex. Finally, the modelling of turbulence also plays an important role in the complex vortical structures on the part of the wing outboard of the crank. The present turbulence model may not be best suited for the complex unsteady vortical structures found in this region.

For flight condition 7 boundary layer measurements were performed at four positions on the left wing (see Chapter 3 and [5-1]). The locations are summarized in Table 5-4. Note that in Figure 5-4 the corresponding positions of the measurement locations on the right wing are shown.

Table 5-4: Boundary-Layer Rake Locations

Boundary Layer Rake	Fuselage Station (FS), in	Butt Line (BL), in
3	302.17	-52.93
4	293.45	-76.22
5	294.59	-96.06
7	295.52	-94.33

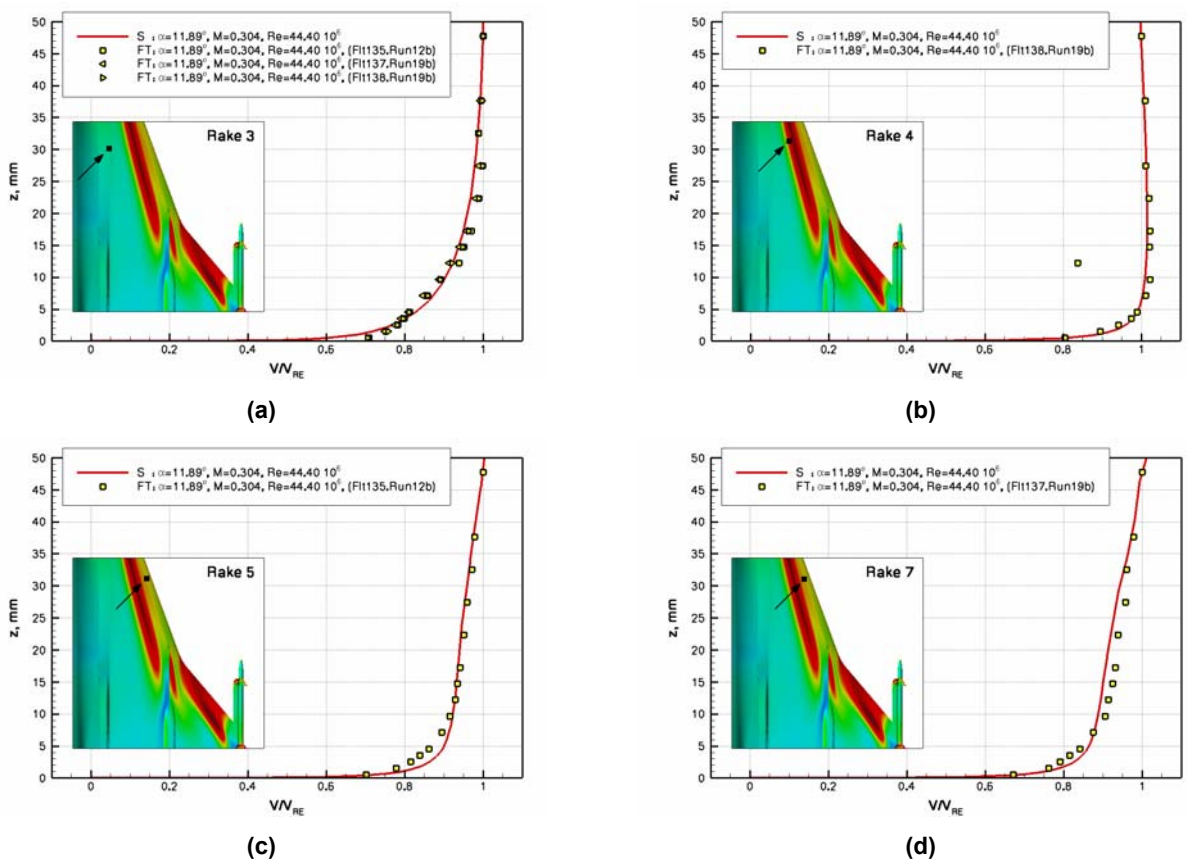

Figure 5-4: Boundary Layer Profiles for Flight Condition 7 (α = 11.89°, M = 0.304 and Re = 44.40 x 10^6).

These location were chosen so that one rake is located well inboard of the inner wing primary vortex (rake 3), one is located underneath the inner wing primary vortex (rake 4) and two are located at the secondary vortex, both underneath (rake 5) and at its separation point (rake 7). Of the 23 available tubes on a rake, 16 active tubes were used for pressure measurements (15 for total pressure measurements and one for static measurements). The ultimate tube was located 2 inches above the surface. The rakes were aligned with the local flow according to an average angle over its height. CFD predictions from the CFL3D code[1] were used to determine this angle.

In Figure 5-4 the boundary layer profiles for flight condition 7 are shown. Note that in this figure the corresponding positions of the measurement locations on the right wing are shown. The agreement between the flight test and the simulation is generally good, especially well inboard of the inner wing primary vortex

(rake 3) and underneath the inner wing primary vortex (rake 4). For the rake locations associated with the inner wing secondary vortex (rake 5 and rake 7), the difference between the flight test and the simulation is slightly larger.

Although in the surface pressure coefficient the presence of a secondary vortex was not that clear, the local velocity seems to be in fairly good agreement in this region. Note also that the deviation between the flight test and the simulation is consistent for the rake locations associated with the inner wing secondary vortex.

Local skin friction measurements were performed for flight condition 19. These local skin friction measurements were performed across the left wing near FS330 using 16 modified Preston tubes (see Chapter 3 and [5-1]). Each total-pressure tube was integrated with a static-pressure port. The tubes were aligned with the local flow based on predictions by the CFL3D code [5-1]. The skin friction values are obtained by relating the pressure change between the total- and static-pressure tubes to the local skin friction. For more details see [5-1].

Figure 5-5 shows the local skin friction coefficient. Note once more that in this figure the corresponding positions of the measurement locations on the right wing are shown. The skin friction coefficient is shown both at the fuselage station used for the flight measurements (FS330) and at approximately the fuselage station where the boundary-layer rakes are located (FS300). At FS330 a good agreement between the flight test and the simulation is shown underneath the inner wing primary vortex, whereas the skin friction coefficient is over predicted underneath the inner wing secondary vortex. At FS300 a similar local skin friction distribution is observed. This distribution is in agreement with the boundary-layer measurements shown in Figure 5-4. In Figure 5-4, one can see that when approaching the surface the slope $d(V/V_{RE})/dz$ of the simulation is larger than the slope of the flight test at rake 5 and rake 7, whereas for rake 4 both agree well. Since the tangential component of the total stress tensor is directly proportional to this slope $d(V/V_{RE})/dz$ and the local skin friction coefficient C_f is the non-dimensional form of the magnitude of this tangential component, a good agreement is to be expected underneath the inner wing primary vortex (rake 4). Correspondingly an over prediction of the local skin friction coefficient is to be expected for the rake locations associated with the inner wing secondary vortex (rake 5 and rake 7).

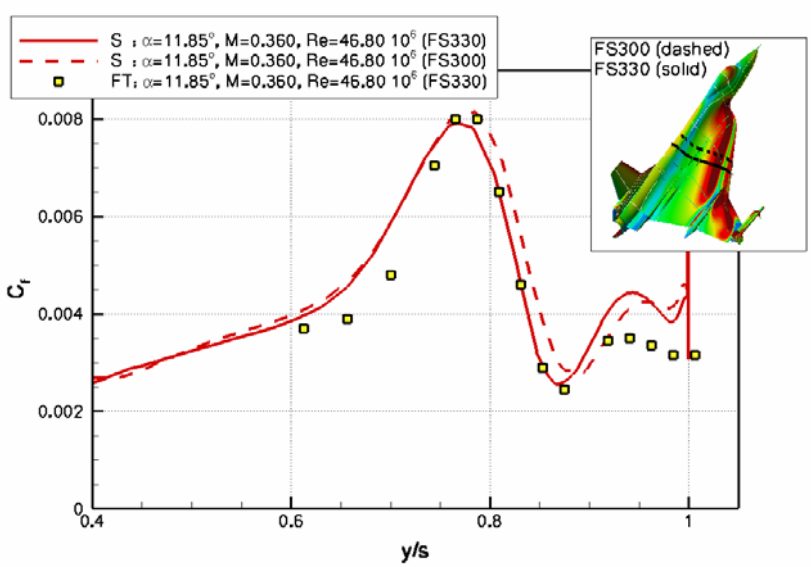

Figure 5-5: Local Skin Friction Coefficient for Flight Condition 19 (α = 11.85°, M = 0.360 and Re = 46.80 x 10^6) at FS300 (dashed line) and FS330 (solid line).

Tufts were used to visualize the surface flow tubes (see Chapter 3 and [5-1]). Six cameras, two mounted atop the vertical tail, one on either side of the fuselage behind the canopy and one in the nose of each dummy missile, were used for recording the tufts data. The time was added to each image by a time-code inserter so that the images could be compared to form a composite and flight test conditions could be established. Images of interest were digitized in a 512- by 480-pixel format for further processing to develop quantifiable video data.

In Figure 5-6, the surface streamlines superimposed on the negative of the original tuft image are shown for flight condition 7 and flight condition 25. The black dots on the wing are video targets that were used for calibrating the images.

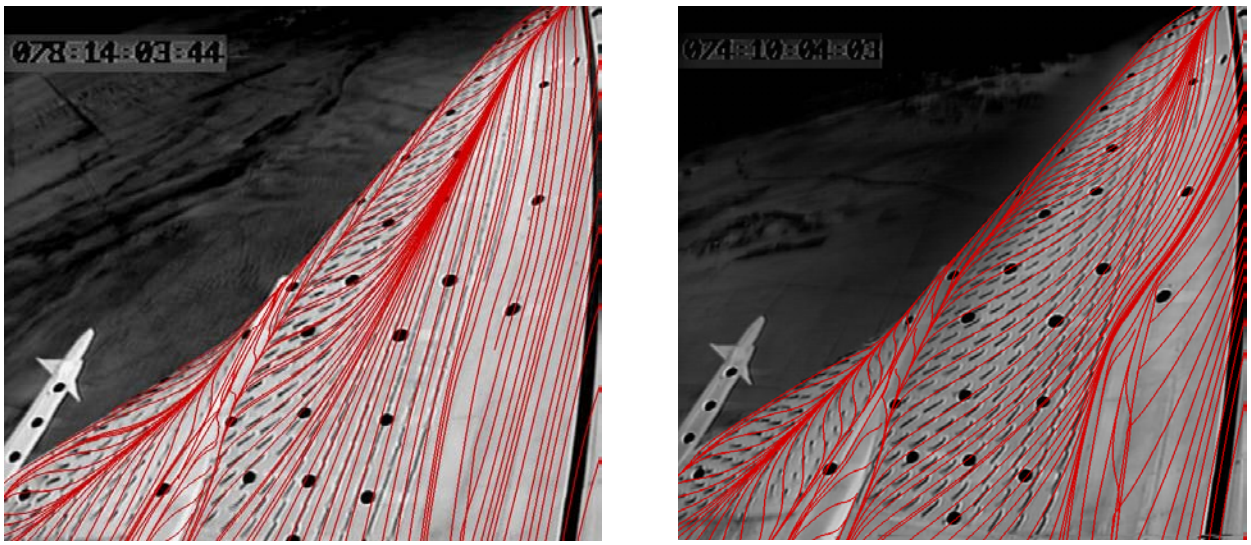

(a) (b)

Figure 5-6: Surface Streamlines Superimposed on the Negative of the Tuft Image for (a) Flight Condition 7 (α = 11.89°, M = 0.304 and Re = 44.40 x 10^6), Flight 145, Run 16b, Video (yr, 1996), 078:14:03:44 (Day:hr:min:sec) and (b) Flight Condition 25 (α = 19.84°, M = 0.242 and Re = 32.22 x 10^6), Flight 144, Run 16b, Video (yr, 1996), 074:10:04:03 (Day:hr:min:sec).

On the part of the wing inboard of the crank the agreement in the flow direction as indicated by the tufts and surface streamlines is good for both flight conditions. Clearly visible are the re-attachment line of the inner wing primary vortex and the separation line of the inner wing secondary vortex.

The agreement in the flow direction as indicated by the tufts and surface streamlines on the part of the wing outboard of the crank is also good for flight condition 25; see Figure 5-6 (b). Note that this flight condition is characterized by a high angle of attack and a strong air dam vortex. For flight condition 7; see Figure 5-6 (a) a less satisfactory agreement is obtained. For both cases, but especially flight condition 7, the tufts have a blurred character on this part of the wing, indicating local unsteadiness of the flow. For both flight conditions a re-attachment line is present.

Finally, the surface streamline pattern obtained for flight condition 7 was further scrutinized; see Figure 5-7. All flight conditions characterized by vortical flow show a surface streamline pattern comparable to that of flight condition 7, although the location of the specific features may differ.

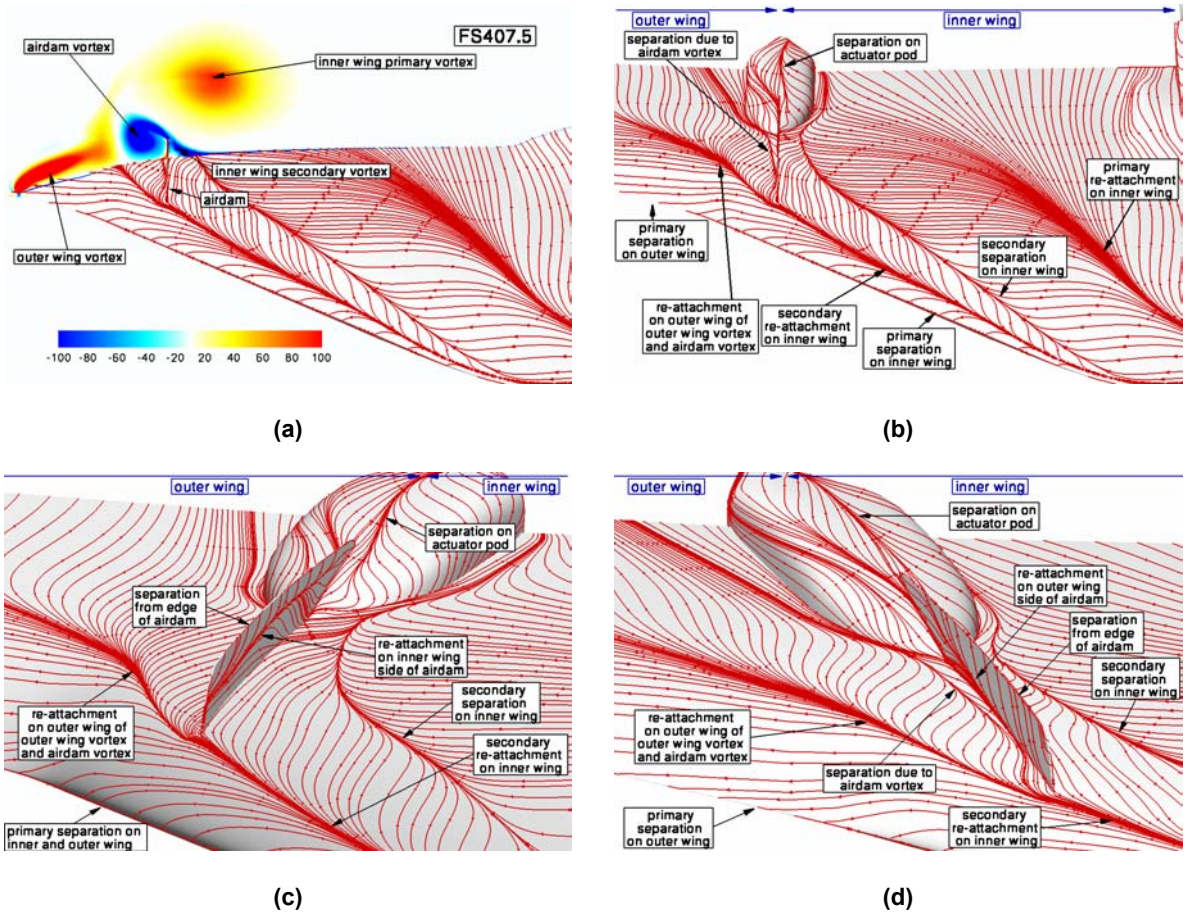

Figure 5-7: Surface Streamline Pattern for Flight Condition 7 (α = 11.89°, M = 0.304 and Re = 44.40 x 10^6): (a) Surface Streamlines with Non-Dimensional Vorticity Magnitude on a Cross-Sectional Plane at FS407.5; (b) Overview of the Surface Streamline Pattern; (c) Detail of the Surface Streamline Pattern on the Part of the Wing Inboard of the Crank; and (d) Detail of the Surface Streamline Pattern on the Part of the Wing Outboard of the Crank.

In Figure 5-7 (a) the vortical flow structures, such as the inner wing primary vortex, the inner wing secondary vortex, the air dam vortex and the outer wing vortex, are shown by means of the non-dimensional vorticity magnitude on a cross-sectional plane at FS407.5. In Figure 5-7 (b), the associated surface streamline pattern is displayed. In Figure 5-7 (c) and Figure 5-7 (d), details on the in board side and the out board side in the air dam region are shown respectively. The surface streamline pattern is composed of the following main elements:

a) *The primary separation on the inner and outer wing*. The flow separates on the wing leading edge. On the part of the wing in board of the crank this separation results in the inner wing primary vortex, whereas on the part of the wing out board of the crank the outer wing vortex is formed.

b) *The primary re-attachment on the inner wing*. At this line the vortical flow associated with the inner wing primary vortex re-attaches on the wing surface. Note that for the present case the inner wing primary vortex lifts off of the surface, resulting in a fanning out of the re-attachment line.

c) *The secondary separation on the inner wing.* Underneath the inner wing primary vortex the flow separates resulting in the inner wing secondary vortex. This separation line starts some distance downstream of the apex of the wing and is present up to the wing trailing edge.

d) *The secondary re-attachment on the inner wing.* At this line the vortical flow associated with inner wing secondary vortex re-attaches to the wing surface. This re-attachment line extends until the leading edge of the air dam.

e) *The re-attachment on the inner wing side of the air dam.* After reaching the air dam the vortical flow resulting from the inner wing secondary vortex re-attaches to the inner wing side of this air dam. Note that this re-attachment line is a continuation of the secondary re-attachment line on the inner wing. When the air dam changes to the actuator pod this re-attachment line stops to exist, and the vortical flow associated with the inner wing secondary vortex re-attaches in the junction between the actuator pod and the wing.

f) *The separation from the edge of the air dam.* The flow separates from the upper edge of the air dam. This separation results in the air dam vortex.

g) *The separation on the actuator pod.* The flow separates from the upper side of the actuator pod. Note that this separation starts before the intersection of the air dam and the actuator pod. The air dam vortex is fed further by the flow coming from this separation.

h) *The re-attachment on the outer wing of the outer wing vortex and the air dam vortex.* At this line the vortical flows associated with both the outer wing vortex and the air dam vortex re-attach.

i) *The separation due to the air dam vortex.* Due to the air dam vortex the flow separates just outboard of the air dam. This separation results in a small vortex in the outboard junction region between the air dam and the wing surface.

j) *The re-attachment on the outer wing side of the air dam.* The vortical flow associated with the small vortex described in (i) re-attaches to the air dam at this line.

Without the presence of the air dam and the actuator pod the vortical flow structure would simply consist of an inner wing primary and secondary vortex and an outer wing vortex. The presence of the air dam and actuator pod significantly complicates the vortical flow structure by introducing a range of other vortices.

5.6 CONCLUSIONS

In the framework of CAWAPI NLR has performed an assessment of NLR's ENFLOW flow simulation system using the F-16XL-1 flight test data. Both the grid generation process and the flow simulation process employed by NLR were part of this assessment.

NLR applied in-house developed (semi-automatic) grid generation algorithms to generate a structured (multi-block) grid. Although most of the algorithms used had become available just before CAWAPI and thus only a limited experience with their application to such a complex configuration as the F-16XL was available, a grid of good quality was generated within a reasonable amount of time. The best practices established during CAWAPI have resulted in a significant reduction of the grid generation time for future projects. At present, once the clean IGES file containing a water tight geometry description of an equally complex configuration is available, a structured (multi-block) grid can be generated in a short period of time. NLR's in-house developed structured (multi-block) grid generation algorithms combine a high grid quality and low through-put time and establish therefore a unique capability in the structured (multi-block) grid generation community.

Steady flow simulations for all seven flight conditions are performed employing the flow solver ENSOLV, which is part of NLR's flow simulation system ENFLOW. All seven flight conditions are simulated within one weekend on NLR's NEC SX5/8B vector computer.

In this chapter only the results obtained for flight condition 7, 19 and 25 are assessed against flight test data, consisting of surface pressure measurements, boundary layer profiles, skin friction measurements and surface flow visualization. Results for the other flight conditions can be found in Chapter 16. The present approach of steady flow simulations utilizing the TNT k-ω model with correction for vortical flows in general predicts the flow well. It should, however, be noted that this turbulence model, primarily validated for the primary vortex on simple sharp-edged delta wings, can be improved for the complex unsteady vortical structures encountered on the F-16XL aircraft. This is suggested by the simulation results for the complex vortical structures on the part of the wing outboard of the crank. In addition, as was seen for the inner wing secondary vortex, grid resolution also plays an important role. To more realistically resolve the complex vortical flow in the region near and outboard of the air dam and actuator pod the introduction of unsteady effects, as was indicated by the tufts images, and the application of more advanced turbulence models that are validated against well-controlled experiments such as performed in the Vortex Flow Experiment II (VFE-II) is required.

CAWAPI has provided NLR with an excellent platform to evaluate its ENFLOW flow simulation system. Through the participation in CAWAPI the grid generation algorithms and the flow algorithms used at NLR have reached a higher Technology Readiness Level for complex fighter configurations.

5.7 REFERENCES

[5-1] Lamar, J.E., Obara, C.J., Fisher, B.D. and Fisher, D.F.: *Flight, Wind-Tunnel, and Computational Fluid Dynamics Comparison for Cranked Arrow Wing (F-16XL-1) at Subsonic and Transonic Speeds*, NASA TP-2001-210629, 2001.

[5-2] *ENFLOW: A Computer Code System for Accurate Simulation of Three-Dimensional Flows*, URL: http://www.nlr.nl/documents/flyers/f222-01.pdf [cited 12 December 2006].

[5-3] Kok, J.C.: *Resolving the Dependence on Free-Stream Values for the k-ω Turbulence Model*, NLR-TP-99295, 1999.

[5-4] Brandsma, F.J., Kok, J.C., Dol, H.S. and Elsenaar, A.: *Leading Edge Vortex Flow Computations and Comparison with DNW-HST Wind Tunnel Data*, NLR-TP-2001-238, 2001.

[5-5] Dol, H.S., Kok, J.C. and Oskam, B.: *Turbulence Modeling for Leading-Edge Vortex Flows*, AIAA-2002-0843, 2002.

[5-6] Kok, J.C., Dol, H.S., Oskam, B. and van der Ven, H.: *Extra-Large Eddy Simulation of Massively Separated Flows*, NLR-TP-2003-200, 2003.

[5-7] de Cock, K.M.J., Kok, J.C., van der Ven, H., Soemarwoto, B.I., Boelens, O.J. and Oskam, B.: *Extra-Large Eddy Simulation for Delta Wings and Space Launchers*, Presented on the 24th International Congress of the Aeronautical Sciences, Yokohama, Japan, August 29 – September 3, 2004.